



PAPER

OPEN ACCESS

RECEIVED
7 March 2022REVISED
23 June 2022ACCEPTED FOR PUBLICATION
13 July 2022PUBLISHED
29 July 2022

Original content from this work may be used under the terms of the [Creative Commons Attribution 4.0 licence](#).

Any further distribution of this work must maintain attribution to the author(s) and the title of the work, journal citation and DOI.



The radiosensitizing effect of platinum nanoparticles in proton irradiations is not caused by an enhanced proton energy deposition at the macroscopic scale

C Behrends^{1,2,3} , C M Bäcker^{1,2,3} , I Schilling² , S Zwiehoff⁴ , J Weingarten² , K Kröninger² , C Rehbock⁴ , S Barcikowski⁴ , J Wulff^{1,3} , C Bäumer^{1,2,3,5} and B Timmermann^{1,3,5,6,7}

¹ West German Proton Therapy Centre Essen (WPE), D-45147 Essen, Germany

² TU Dortmund University, Department of Physics, D-44221 Dortmund, Germany

³ University Hospital Essen, West German Cancer Centre (WTZ), D-45147 Essen, Germany

⁴ University of Duisburg-Essen, Technical Chemistry I, (CENIDE), (ZMB), D-45141 Essen, Germany

⁵ German Cancer Consortium (DKTK), D-69120 Heidelberg, Germany

⁶ University of Duisburg-Essen, Faculty of Medicine, D-45147 Essen, Germany

⁷ University Hospital Essen, Department of Particle Therapy, D-45147 Essen, Germany

E-mail: carina.behrends@uk-essen.de

Keywords: proton therapy, noble metal nanoparticles, radiosensitizing effect, energy deposition

Abstract

Objective. Due to the radiosensitizing effect of biocompatible noble metal nanoparticles (NPs), their administration is considered to potentially increase tumor control in radiotherapy. The underlying physical, chemical and biological mechanisms of the NPs' radiosensitivity especially when interacting with proton radiation is not conclusive. In the following work, the energy deposition of protons in matter containing platinum nanoparticles (PtNPs) is experimentally investigated. **Approach.** Surfactant-free monomodal PtNPs with a mean diameter of (40 ± 10) nm and a concentration of $300 \mu\text{g ml}^{-1}$, demonstrably leading to a substantial production of reactive oxygen species (ROS), were homogeneously dispersed into cubic gelatin samples serving as tissue-like phantoms. Gelatin samples without PtNPs were used as control. The samples' dimensions and contrast of the PtNPs were verified in a clinical computed tomography scanner. Fields from a clinical proton machine were used for depth dose and stopping power measurements downstream of both samples types. These experiments were performed with a variety of detectors at a pencil beam scanning beam line as well as a passive beam line with proton energies from about 56–200 MeV. **Main results.** The samples' water equivalent ratios in terms of proton stopping as well as the mean proton energy deposition downstream of the samples with ROS-producing PtNPs compared to the samples without PtNPs showed no differences within the experimental uncertainties of about 2%. **Significance.** This study serves as experimental proof that the radiosensitizing effect of biocompatible PtNPs is not due to a macroscopically increased proton energy deposition, but is more likely caused by a catalytic effect of the PtNPs. Thus, these experiments provide a contribution to the highly discussed radiobiological question of the proton therapy efficiency with noble metal NPs and facilitate initial evidence that the dose calculation in treatment planning is straightforward and not affected by the presence of sensitizing PtNPs.

1. Introduction

Based on the idea of enriching tumors with high-*Z* materials, biocompatible noble metal nanoparticles (NPs) are of great interest in radiobiological research (Schuemann *et al* 2020). The seminal study of the NPs' radiosensitizing effect was achieved by Hainfeld *et al* (2008), who demonstrated a dose enhancement effect with x-rays in malignant tumors by gold nanoparticles (AuNPs) using a mouse model. Further experiments and

simulations indicated the dose enhancement effect of AuNPs in combination with ionizing radiation, outlining the promising application of NPs in radiotherapy (Mesbahi 2010, Butterworth *et al* 2012).

In addition to photons, metal NPs or metallic complexes can be combined with particle radiation to potentially induce an enhancement of the radiotherapeutic effect (Usami *et al* 2005, 2008, Kim *et al* 2010, Lacombe *et al* 2017). Using *in vitro* studies, Polf *et al* (2011) demonstrated the increased biological effectiveness of protons with AuNPs: A 15%–20% increased efficiency in killing prostate tumor cells was shown in the presence of AuNPs. Furthermore, Li *et al* (2016) described a dependence of radiosensitizing effects of AuNPs on linear energy transfer (LET) of proton fields.

The mechanism behind the potentially enhanced proton therapy efficiency due to the radiosensitizing effect of metal NPs has not been fully understood yet (Schuemann *et al* 2020). On the one hand, due to the large atomic number Z of noble metal NPs, particle-induced x-ray emission (PIXE) was assumed as an explanation for the dose enhancement in the surrounding tumor tissue (Kim *et al* 2010, Polf *et al* 2011). However, Dollinger (2011) argued based on stopping power calculations that the energy imparted by protons to the NPs is expected to be too low to cause a PIXE-based enhancement effect.

On the other hand, the secondary electrons induced by the protons on their primary track may contribute. Sech *et al* (2012) postulated an energy conversion of the secondary electron energy into Auger de-excitation in the heavy atoms: they suggested that Auger electrons emitted by secondary electron induced inner-atomic Auger cascades in the NPs cause the radiolysis of the surrounding water molecules leading to free hydroxyl radicals. By assuming that the conversion of energy may cause the enhancement effect, they precluded an increased proton energy deposition. A local microscopic dose effect enhancement around the NPs due to Auger electrons was investigated and confirmed in Monte Carlo studies (Wälzlein *et al* 2014, Cho *et al* 2016, Lacombe *et al* 2017).

In contrast to previous approaches, Sicard-Roselli *et al* (2014) explained the radiosensitizing effect of AuNPs—though with photon radiation—via a catalytic process occurring at the interface between the NPs and water molecules. The corresponding chemical reactions increase the effectiveness of the radiolysis of water molecules in the immediate vicinity of the NPs.

While there is a discrepancy concerning the interpretation of the process which causes increased radiolysis of water, the important contribution of the resulting reactive oxygen species (ROS) to the enhanced radiotherapy effect has been demonstrated in several works (Kim *et al* 2012, Li *et al* 2016, Schlathölter and Eustache 2016, Smith *et al* 2017). Furthermore, Zwiehoff *et al* (2021) demonstrated that the enhancement in proton therapy with platinum NPs (PtNPs) is a surface- and not a mass-dependent effect, further indicating that a surface-driven catalytic process is involved.

In order to provide a contribution to the discussed mechanisms, this study intends to verify experimentally that radiosensitizing effects by PtNPs are not correlated with an increased proton energy deposition at the macroscopic scale. For that, surfactant-free PtNPs were produced and tissue-like samples with (PtNP samples) and without injected PtNPs (nonPtNP samples) were manufactured. For confirmation of the fact that the NPs in the samples can potentially increase proton therapy efficiency, the radiosensitizing effect of equivalent colloidal PtNPs in terms of increased ROS generation under proton irradiation was verified. Furthermore, a clinical computed tomography (CT) scan was used to investigate the properties of the PtNP and nonPtNP samples. To investigate the aspects in the energy domain for the radiosensitizing effect of these PtNPs, proton beam measurements with quality assurance devices and three types of experimental setups were performed for the PtNP and nonPtNP samples and compared in terms of the proton dose and energy distribution downstream of the samples. To further assess the impact of PtNPs on treatment planning, spot sizes were analyzed to compare proton scattering effects with and without PtNPs.

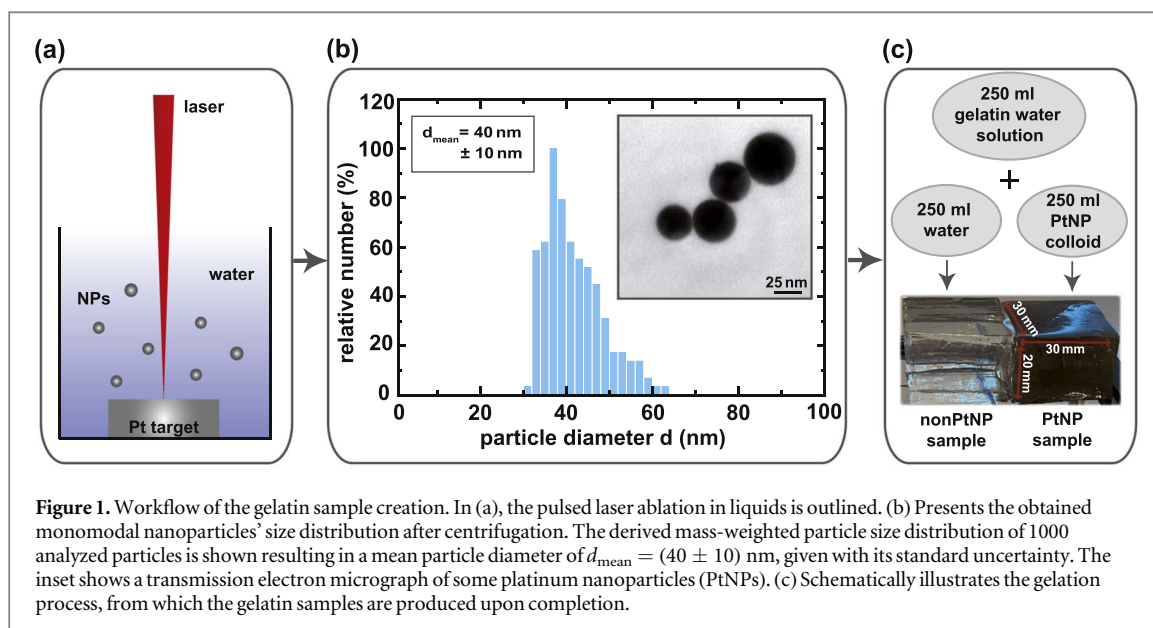
Overall, this study examines in detail the energy balance downstream of the PtNP and nonPtNP samples in the beam path and provides the experimental evidence that the underlying radiosensitizing effect cannot be explained by an increased proton energy deposition at the macroscopic scale.

2. Methods

2.1. Manufacturing process of the samples

2.1.1. Pulsed laser ablation in liquids

Surfactant-free PtNPs were produced through pulsed laser ablation (picosecond Nd:YAG laser, Ekspla (Vilnius, Lithuania), Atlantic Series, 10 ps, 1064 nm, 9.6 mJ, 100 kHz) of a platinum target placed in a batch chamber filled with ultra pure water (electrical resistivity: 18.2 M Ω cm at 25 °C) (Waag *et al* 2021). Figure 1(a) presents a sketch of this method. Focusing of the laser beam was done by an f -theta lens. Utilizing a galvanometric scanner, the focused beam was spirally scanned over the target. A bimodal particle size distribution was obtained through 15 min ablation with a nominal laser fluence of 6.1 J cm⁻² on the surface of the target.



2.1.2. Centrifugation

To get a monomodal size distribution, the ablated colloid was centrifuged (Hettich, 295 g, 35 min) and the generated pellet was used to isolate the PtNPs. For this, the pellet was diluted with ultra pure water, yielding a mass concentration of $600 \mu\text{g ml}^{-1}$. A transmission electron micrograph of the PtNPs and the obtained particle diameter distribution with a mean value of $d_{\text{mean}} = (40 \pm 10)$ nm is shown in figure 1(b).

2.1.3. Gelation process

The gelation process of the samples with and without PtNPs is pictured in figure 1(c). 25 g gelatin were left to swell in 250 ml cold ultra pure water for 10 minutes. While stirring, the solution was heated to 40°C until the gelatin dissolved. Then, 250 ml of water or colloidal PtNPs, each previously tempered to 30°C , were added under stirring to the gelatin solution. The mixture with PtNPs resulted in a final concentration of $300 \mu\text{g ml}^{-1}$ (a percentage weighting of platinum to gelatin mass of 0.03 wt%). Both mixtures were poured into templates, resulting in a filling height of 20 mm. After curing, the resulting gels were cut into cuboids which yield the PtNP and nonPtNP samples. They have lateral dimensions of about $30 \times 30 \text{ mm}^2$ and a vertical dimension of roughly 20 mm given by the filling height (see figure 1(c)). The latter indicates the distance in the material traversed by the beam. Since this sample thickness is difficult to determine accurately due to the soft properties of gelatin, the ratio of this sample thickness H and the sample's water equivalent thickness (WET) (Zhang and Newhauser 2009) are used in the following.

2.2. Verification of ROS generation of PtNPs during proton irradiation

In order to additionally verify the enhancement effect of the samples' PtNPs in preparation for the following experiments, the ROS generation during proton irradiation was quantified with water phantoms. An absorbed dose of 5 Gy and the setup described in Zwihehoff *et al* (2021) was used. Briefly, terephthalic acid (TA) was added to the colloidal PtNPs before irradiation. During proton irradiation, the generated hydroxyl radicals react with the TA forming 2-hydroxyterephthalic acid (2-OH-TA), whose fluorescent signal could be measured to determine the concentration of hydroxyl radicals. To obtain the fluorescent intensity, the PtNPs were precipitated directly after the irradiation, avoiding any cross or quenching effects. Colloidal PtNPs were created in concentrations of 50, 100, 200 and $300 \mu\text{g ml}^{-1}$ having a total available surface area from 3 to $17 \text{ cm}^2 \text{ ml}^{-1}$. Figure 2 presents the effect of the increasing PtNPs' concentration on the generated 2-OH-TA. A higher concentration of PtNPs leads to an increased production of 2-OH-TA in comparison to the reference, up to an increase by a factor greater than 2 at the concentration of $300 \mu\text{g ml}^{-1}$. At all concentrations, the samples with colloidal PtNPs were able to generate more radicals than the reference without PtNPs, indicating a sensitizing effect of the implemented PtNPs.

2.3. Treatment planning study

In order to verify the homogeneity and geometric properties of the samples, x-ray acquisitions of two PtNP and two nonPtNP samples were performed with a Brilliance Big Bore scanner (Philips, Hamburg, Germany). The samples of each type were placed diagonally to the CT axis to mitigate artifacts, e.g. reconstruction artifacts

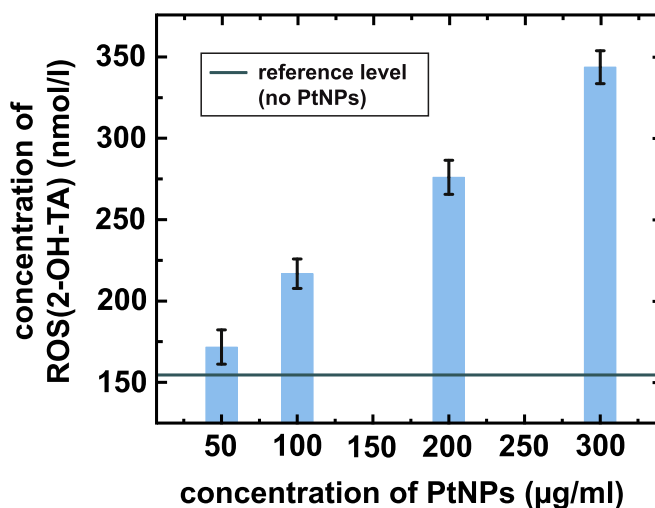


Figure 2. Generated 2-OH-TA concentration during proton irradiation of platinum nanoparticles (PtNPs) in presence of terephthalic acid (TA). PtNPs' concentration was increased while irradiation fields were kept constant (absorbed dose of 5 Gy). The standard uncertainties shown with the error bars arrive from the measurement of nine independent samples. The horizontal line at 155 nmol l^{-1} represents the concentration of 2-OH-TA in the absence of PtNPs during proton irradiation serving as the reference level.

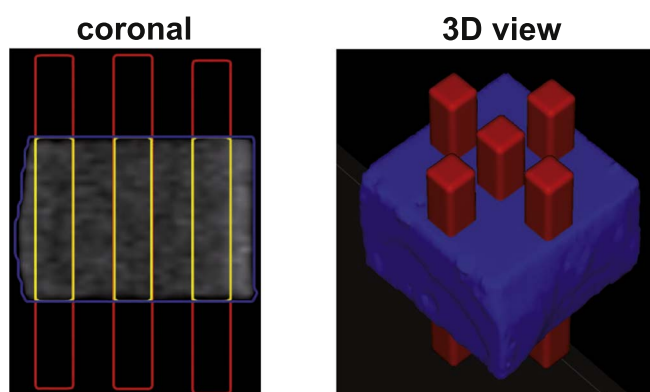


Figure 3. Method for identifying the sample thicknesses using help structures: matchstick-shaped volumes (red) with known edge lengths are used to determine the sample's thickness via their intersection volume (yellow) with the sample's outer contour (blue). The coronal view with the contours is shown on the left and the 3D view on the right.

induced by the sharp corners. A high resolution scan protocol with a reconstructed lateral pixel size of 0.65 mm and a tube voltage of 80 kV was used. Subsequently, the outer contour of the phantoms was generated gray level based in the clinical treatment planning system RayStation 6.99 (RaySearch Laboratories, Stockholm, Sweden). The CT numbers CT_{num} in Hounsfield Units (HU) were evaluated in regions of interest (ROIs) contracted by 5 mm with respect to the outer samples' contours. The CT contrast of the NPs is defined as the difference of the mean CT_{num} of the samples: $\Delta \overline{CT}_{\text{num}} = \overline{CT}_{\text{num}}(\text{PtNP}) - \overline{CT}_{\text{num}}(\text{nonPtNP})$.

The so-obtained mean CT contrast $\Delta \overline{CT}_{\text{num}}$ was used to determine the physical thicknesses of the samples as accurately as possible. For that, the samples' outer contours were again delineated based on their gray levels under consideration of $\Delta \overline{CT}_{\text{num}}$. The outer contours were defined at the 50% level of the average CT numbers in the contracted ROIs. Thus, 50% of $\Delta \overline{CT}_{\text{num}}$ was used for the specification of the samples volumes. To identify the samples' physical thicknesses, well-defined matchstick shaped volumes as presented in red in figure 3 with a small cross section overlapping with the sample volumes in beam direction were used as help structures. By determining the intersection (yellow contours in figure 3), the long edge length of the intersection volume (which corresponds to the sample thickness) could be determined via the known volume and edge lengths of the small cross sectional area. The mean thickness of each sample type was established over five repetitions while varying the lateral position of the help structures (see figure 3). However, since this thickness depends on the HU-scale, its gray scale independent thickness ratio H was calculated with

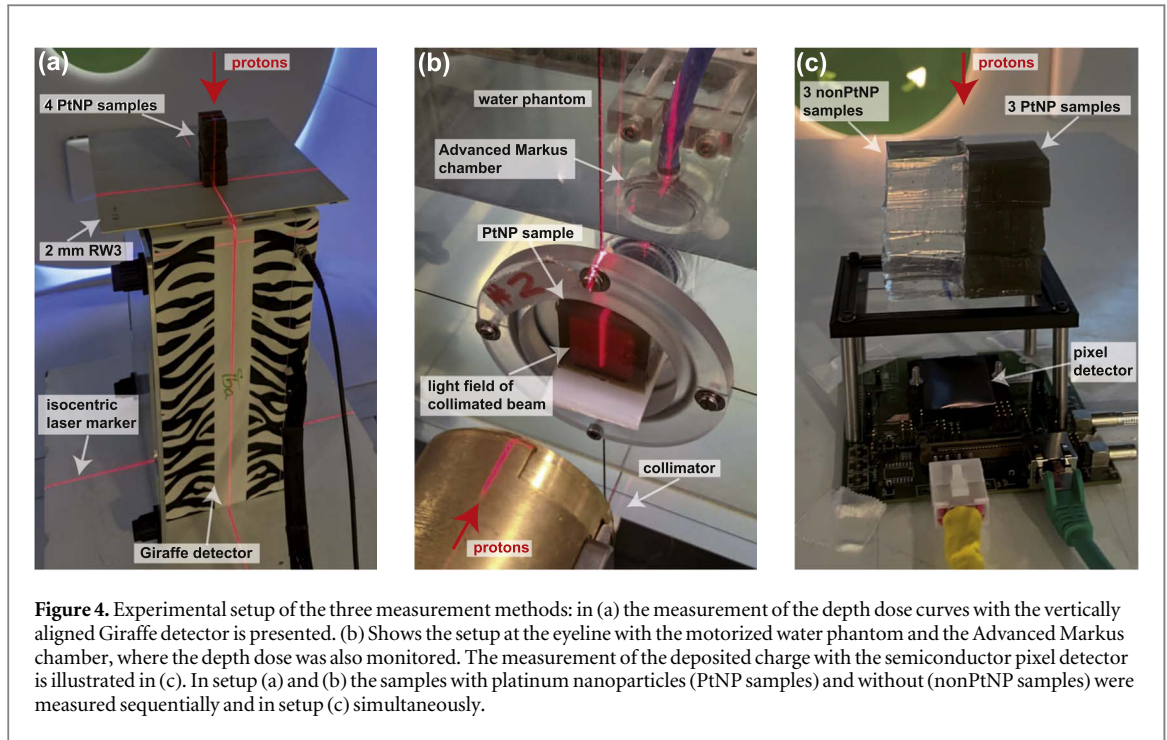


Figure 4. Experimental setup of the three measurement methods: in (a) the measurement of the depth dose curves with the vertically aligned Giraffe detector is presented. (b) Shows the setup at the eyeline with the motorized water phantom and the Advanced Markus chamber, where the depth dose was also monitored. The measurement of the deposited charge with the semiconductor pixel detector is illustrated in (c). In setup (a) and (b) the samples with platinum nanoparticles (PtNP samples) and without (nonPtNP samples) were measured sequentially and in setup (c) simultaneously.

$$H = \frac{h_{\text{PtNP}}}{h_{\text{nonPtNP}}}, \quad (1)$$

where h_{PtNP} and h_{nonPtNP} are the calculated mean sample thicknesses at a sample-specific gray level window. With the help of H , the necessity of exactly estimating the physical sample thickness and the attendant uncertainties, as well as possible height compressions when stacking the samples, were circumvented.

Based on the determined CT contrast from the imaging study, the influence of PtNPs applied in the tumor on treatment planning in terms of dose calculation was investigated. For this purpose, three exemplary pediatric patients with brain tumors (two ependymoma and one medulloblastoma) with slightly different localizations were selected. On a copy of the original planning CT and using the clinical calibration curves, the density of the planning target volume (PTV) was overwritten according to the density with the additional determined CT contrast $\Delta \overline{CT}_{\text{num}}$ above. Subsequently, the original highly conformal dose distribution in the PTV was recalculated on the CT with the overwritten PTV density. The difference in the PTV's dose coverage $\Delta D_{98\%}$ (the dose of the PTV, which is at least delivered to 98% of the PTV's volume) was calculated with $\Delta D_{98\%} = D_{98\%}(\text{original})/D_{98\%}(\text{overwritten}) - 1$, where $D_{98\%}(\text{original})$ is the PTV's dose $D_{98\%}$ with original density and $D_{98\%}(\text{overwritten})$ the PTV's dose $D_{98\%}$ with overwritten density.

2.4. Measurements of depth dose and energy deposition

The experiments were performed at the West German Proton Therapy Centre Essen (WPE), a clinical proton therapy center, equipped with an IBA ProteusPlus proton therapy system (IBA PT, Louvain-La-Neuve, Belgium) based on a 230 MeV isochronous cyclotron. Both, the pencil beam scanning (PBS) technique as well as a passive treatment technique of an IBA ProteusPlus proton therapy system (IBA PT, Louvain-La-Neuve, Belgium) were used as elucidated in the following.

In order to measure the energy balance outside the samples in multifaceted ways, three independent measurement setups and detectors pictured in figure 4 were used. These measurements allow to infer the energy deposition of the protons in the samples.

2.4.1. Multi-layer ionization chamber Giraffe

A clinical PBS beam line equipped with an IBA PBS dedicated nozzle was used to measure the depth dose distribution downstream of the samples. A multi-layer ionization chamber (MLIC) Giraffe detector (IBA Dosimetry, Schwarzenbruck, Germany) with an electrode diameter of 12 cm was captured with mono-energetic single co-axial pencil beam spots (Bäumer *et al* 2015). The MLIC consists of 180 air-filled ionization chambers with a distance of 2 mm in beam direction, which was effectively reduced by measuring with and without an additional cover of 1.2 mm WET. In order to be able to position the phantoms and align them to the beam direction, the protons were applied from a gantry angle of 0° and the detector was set up vertically (see figure 4(a)). In addition, a solid water phantom (RW3-plates, type SP34 IBA Dosimetry, composition: 98%

polystyrene + 2% TiO₂) with a physical thickness of 2 mm ($WET = 2.06$ mm) was placed on the detector to allow stable positioning of the samples. The samples were aligned with the isocentric laser marker. The combination of thin spots with large-area stacked ionization chambers allows to study the WET of the samples within a small cross section.

Depth dose curves (DDCs) based on charge count values in the MLIC were measured downstream of the PtNP and nonPtNP samples. To be sensitive to possible pull-backs of the Bragg peak by the NPs, the thickness of the sample should be as large as possible. In order to investigate also the influence of proton energy, two samples of each type were stacked for 100, 140, 170 and 200 MeV, whereas measurements at 200 MeV were also made with four stacked samples. The single proton spots have corresponding initial spot widths (σ) of 5.4 mm, 4.1 mm, 3.7 mm and 3.1 mm.

2.4.2. Plane parallel ionization chamber in motorized water phantom

The same experimental design with a different type of proton field and different type of detector was pursued with the PtNP and nonPtNP samples at a dedicated eye treatment beam line (IBA PT, Louvain-La-Neuve, Belgium; hereafter abbreviated as eyeline), which is similar to the one described by Slopsema *et al* (2013). The horizontal beam line features the single-scattering mode with residual proton ranges up to 35 mm. Consequently, only one sample with and without PtNPs was used for this setup (see figure 4(b)). Collimated 20×20 mm² fields with a residual range of 35 mm and a modulation width of 35 mm (R35M35), and with a residual range of 27 mm and a modulation of 28 mm (R27M28) were used for the measurements. The kinetic energies upstream of the samples for these two field configurations vary between 56 and 64 MeV for the highest energy in the proton field based on the data base of the National Institute of Standards and Technology (NIST) (Berger *et al* 2005). The light field of the eyeline on the PtNP sample can be seen in figure 4(b).

The relative DDCs of the PtNP and nonPtNP samples were measured with a plane parallel ionization chamber, the PTW34045 Advanced Markus chamber (PTW, Freiburg, Germany), which was placed in the center of the quadratic field shape. An additional reference chamber (Semiflex 31 010, PTW, Freiburg, Germany) was used for dose rate normalization. A modified motorized MP3 XS water phantom (PTW, Freiburg, Germany) with an extra thin entrance window (WET of Markus chamber and phantom window = 2.22 mm) enabled step sizes of 0.1 mm in depth. The positioning of the PtNP sample in front of the thin entrance window with the help of an additional pad is shown in figure 4(b).

2.4.3. Pixelated semiconductor detector

For the third measurement setup demonstrated in figure 4(c), an innovative experimental apparatus consisting of a pixelated semiconductor counting-mode detector designed for high energy physics tracking experiments was utilized at a clinical PBS beam line, which was described in section 2.4.1. Here, the deposited energy of the protons in the detector was determined, allowing a measurement of energy loss, independent of the ionization chamber based setups mentioned above.

The chosen ATLAS IBL pixel detectors are hybrid detectors, with a 200 μm thick n-in-p silicon sensor, segmented in 80×336 pixels with a size of 250×50 μm^2 (Grinstein 2013), which is bump bonded to a FE-I4B readout chip (Garcia-Sciveres *et al* 2011). A time over threshold signal with a 4-bit storage provides information about the number of electrons generated in the sensor, which gives the deposited energy by multiplying with the mean excitation energy for an electron-hole pair in silicon (3.6 eV (Klein 1968)). The deposited energy in the sensor yields the stopping power for the protons in 200 μm silicon. Threshold and gain of each readout channel were optimized for energy depositions between 100 keV and about 750 keV, which is close to the maximum charge the readout chip can register and fits the stopping power range of the protons entering the sensor. The hits on the sensor were spatially and temporally clustered to assign them to one initial proton. Of these, only single hit clusters were analyzed, allowing only events in which the proton has deposited its entire energy in one pixel. Subsequently, the mean value of the distribution of the deposited energy in the sensor was determined. Generally, the efficiency of the detector to register individual protons exceeds 99.9% (Weingarten 2012).

Homogeneous fields with lateral dimensions of 25×25 mm² were used. PtNP and nonPtNP samples were irradiated side by side on the sensor to investigate the difference in energy deposition with and without the presence of PtNPs. The described analysis was performed in central ROIs downstream of the samples to exclude artifacts in the edge regions.

In addition, the spot sizes, defined as the sigma of the Gaussian-shaped spot profiles, were determined to investigate the effects from PtNPs on the scattering of protons. For this purpose, the time structure of the hit positions in the PBS field (step and shoot technique) was extracted. A 1D Gaussian function was fitted to each spot profile in the direction of the longer pixel edge as a summation of hits along all short pixel edges gives a higher hit statistic for each fit data point. Only spots close to the center of the respective sample were selected to exclude effects at the interface between the sample types or the detector edge. The mean spot size $\bar{\sigma}_{\text{spot}}$ of the spots in the evaluated region downstream of each sample was calculated for every measurement.

Three samples of each type were exposed to 100 MeV protons, one sample each to 110 and 120 MeV and additionally four stacked samples each to 120 MeV. For the setups with one sample each, an additional buildup of $WET = 56.2$ mm consisting of one clinical range shifter (material: Polymethyl methacrylate, $WET = 51$ mm) and an RW3-plate of $WET = 5.2$ mm was placed in front of the samples to obtain the appropriate range of energy deposition in the sensor. For each setup except the one at 120 MeV and four stacked samples, the measurement with both samples was performed twice. For all measurements, the pixel detector was located in the dose gradient proximal to the peak position of the Bragg curve. Depth positions relative to R_{80} (the range in water at which the distal dose in the Bragg peak has reached 80%) were: $0.8 R_{80}$ for 100 MeV, $0.9 R_{80}$ for 110 MeV, $0.7 R_{80}$ for 120 MeV and one sample, and $0.8 R_{80}$ for 120 MeV and four samples.

2.5. Data interpretation

To evaluate the range measurements (setups in figures 4(a) and (b)) the DDCs were normalized and the dimensionless energy dependent quantity water equivalent ratio WER was evaluated (Zhang and Newhauser 2009). The WER is the WET normalized to the physical thickness h_{sample} :

$$WER_{\text{sample}}(E) = \frac{R_{80, \text{no sample}}(E) - R_{80, \text{sample}}(E)}{h_{\text{sample}}} = \frac{WET_{\text{sample}}(E)}{h_{\text{sample}}}. \quad (2)$$

Here the index 'sample' corresponds to 'nonPtNP' or 'PtNP', E is the initial kinetic proton energy and R_{80} is the range in water with or without a sample in beam path, respectively. To elaborate deviations between the depth dose curves after passing the PtNP and nonPtNP samples, $WER_{\text{ratio}}(E)$ as the ratio between the characteristic $WER_{\text{sample}}(E)$ was calculated with the thickness ratio H (equation (1)) as follows:

$$WER_{\text{ratio}}(E) = \frac{WER_{\text{nonPtNP}}(E)}{WER_{\text{PtNP}}(E)} = H \cdot \frac{WET_{\text{nonPtNP}}(E)}{WET_{\text{PtNP}}(E)}. \quad (3)$$

Based on this definition, an increased stopping power for protons by PtNPs would yield a WER_{ratio} less than 1.

To quantify the effect of nuclear interactions of the protons with the PtNPs, the deviation of the DDCs' charge counts for each sampling point of the DDC with and without PtNPs was determined using the measurements with the Giraffe. For this purpose, the point-wise ratio of the counts downstream of the nonPtNP sample, cnt_{nonPtNP} , to the counts downstream of the PtNP sample, cnt_{PtNP} , was calculated:

$$DDC_{\text{dev}} = \frac{cnt_{\text{nonPtNP}}}{cnt_{\text{PtNP}}} - 1. \quad (4)$$

Hence, positive values of DDC_{dev} indicate a local dose decrease and negative values of DDC_{dev} a local dose enhancement of the proton beam in the presence of PtNPs. Since deviations in the physical sample thicknesses leading to shifts in the peak region would result in large differences and misinterpretation, this analysis was performed in the entrance plateau up to the proximal R_{50} position (range at which the proximal dose has reached 50%). A corresponding analysis of the measurements at the eyeline was not possible, because only relative values related to the reference chamber measuring dose rate fluctuations were available.

The pixelated semiconductor sensor provides information about the deposited energy of the individual protons in the sensor. To compare the mean deposited energies downstream of the PtNP and nonPtNP samples in the sensor, $\overline{E_{\text{dep, PtNP}}}(E)$ and $\overline{E_{\text{dep, nonPtNP}}}(E)$, the energy dependent ratio $E_{\text{dep, ratio}}$ was formed:

$$E_{\text{dep, ratio}}(E) = \frac{\overline{E_{\text{dep, nonPtNP}}}(E)}{\overline{E_{\text{dep, PtNP}}}(E)}. \quad (5)$$

Assuming that the samples have the same physical thickness, one would expect a value of $E_{\text{dep, ratio}}$ less than 1 if the protons deposit more energy in the PtNP sample, since they would correspondingly deposit more energy in the downstream positioned sensor according to the Bethe Bloch formalism (Bethe 1930, Bloch 1933).

For the analysis of possible scattering effects of the protons at the PtNPs, the determined mean spot sizes, $\overline{\sigma_{\text{spot, PtNP}}}(E)$ and $\overline{\sigma_{\text{spot, nonPtNP}}}(E)$, downstream of the respective sample were also put into relation.

$$\sigma_{\text{spot, ratio}}(E) = \frac{\overline{\sigma_{\text{spot, nonPtNP}}}(E)}{\overline{\sigma_{\text{spot, PtNP}}}(E)}. \quad (6)$$

With this definition, a value less than 1 would indicate an increased proton scattering in the measurements with PtNPs.

2.6. Uncertainty analysis

The uncertainties were evaluated as type A and B uncertainties based on the guide to the expression of uncertainty in measurement (Joint Committee for Guides in Metrology 2008). For assessing the uncertainties on the experimental determination of WER_{ratio} (equation (3)), the individually contributing uncertainties of H and the WET of the samples were evaluated: the ratio of sample thickness H was determined in the CT image for each

sample species multiple times, resulting in the statistical type A standard uncertainty of one standard deviation σ_H equal to 0.021.

To determine the uncertainties on the measurements of the DDCs using known quantities, the uncertainties on the *WET* were analyzed for the Giraffe setup and the uncertainties on the R_{80} were analyzed for the water tank setup at the eyeline. Reproduction measurements with the Giraffe have yielded a type A uncertainty of 0.004 mm and measurements with respect to resolution on the *WET* have yielded a type B uncertainty of 0.02 mm. The total uncertainty of the *WET* with the Giraffe was 0.02 mm, resulting from quadratic addition, and is therefore smaller than the distance between neighboring chambers in the MLIC. Using the same setup with the water tank and the Advanced Markus chamber at the eyeline, the range was measured many times over months, allowing the uncertainty about reproducibility and thus the uncertainties of the beam and the motorized phantom to be determined as 0.11 mm. Consequently, the uncertainty on WER_{ratio} could be calculated according to Gaussian error propagation. For all measured energies with the Giraffe as well as at the eyeline, a standard uncertainty of $\sigma_{WER_{\text{ratio}}} = 0.022$ was obtained.

Experimental uncertainties on the deposited energy in the semiconductor sensor were estimated using response measurements of homogeneity and reproducibility. For this purpose, the deposited energy on the sensor downstream of a step phantom of nine different thicknesses was measured twice and another two times after the step phantom was rotated by 180° . When comparing the deposited energy of the measurement repetitions and downstream of the steps of the phantom, a type A uncertainty of 1.09% on the mean deposited energy in the semiconductor detector could be determined. The uncertainty on $E_{\text{dep,ratio}}$ was determined according to quadratic addition of the relative uncertainties for the mean deposited energy for the respective measurements. The maximum value for the standard uncertainty of $E_{\text{dep,ratio}}$ is $\sigma_{E_{\text{dep,ratio}}} = 0.016$.

Based on the knowledge that the samples' thicknesses may vary slightly, the corresponding effect on $E_{\text{dep,ratio}}$ is conservatively estimated in a second uncertainty analysis: assuming that one nonPtNP sample is $h_{\text{nonPtNP}} = 20$ mm thick, the thickness of one PtNP sample is determined by the factor H , taking into account the uncertainty of H : $h_{\text{PtNP}} = h_{\text{nonPtNP}} \cdot (H \pm \sigma_H)$. This assumption is based on the NIST data (Berger *et al* 2005) and yields a $\pm 1\sigma$ confidence interval for the ratio of the deposited energies in the sensor, which is [0.972; 1.036] at 100 MeV, [0.989; 1.013] at 110 MeV, [0.995; 1.007] at 120 MeV with one sample and [0.977; 1.029] at 120 MeV with four stacked samples. The corresponding deviations to the value 1 were considered as a second uncertainty.

In the spot size analysis, the experimental uncertainty downstream of the PtNP and nonPtNP sample was given by the standard uncertainty of the spot sizes of different positions for the respective measurement. For the ratio, the total uncertainty was calculated using Gaussian error propagation, with the largest value being $\sigma_{\sigma_{\text{spot,ratio}}} = 0.014$.

3. Results

3.1. Impact on treatment planning

A transversal CT slice to verify the sample properties is shown in figure 5. Based on the contracted ROIs highlighted in green in figure 5, a contrast $\Delta \overline{CT}_{\text{num}}$ of about 6 HU was found, so $\overline{CT}_{\text{num}}$ of the PtNP samples is larger than that of the nonPtNP samples (see section 2.3). Therefore, an offset of 3 HU was used for contouring the 50% sample level outline when determining the physical sample thickness. The analysis revealed the ratio $H = 0.997(21)$. Since the outer contours presented in figure 5 are gray level based with largely straight parallel lines, almost homogeneous sample thicknesses were assumed.

This CT contrast $\Delta \overline{CT}_{\text{num}}$ from the PtNPs applied to voxels of the target volume in three clinical pediatric brain tumor plans, would result in a mean density increase of 0.005 g cm^{-3} in the PTV. The values of the difference in dose coverage $\Delta D_{98\%}$ of the PTV due to the density change resulted in 0.04%, 0.16% and -0.13% for the tested patients.

3.2. WER comparison from depth dose measurements

The results of the depth dose distributions with varying proton energies and field configurations with and without PtNPs are shown in figure 6. Since it is known from the CT analysis that the PtNP and nonPtNP samples are potentially not equally thick (see section 3.1), the measured values were in first order corrected with the known ratio of H . With this, the DDCs of the nonPtNP and the PtNP samples for the mono-energetic fields in figure 6(a) as well as the energy modulated fields in figure 6(b) are consistent. The experiment with the highest energy of 200 MeV and four stacked samples of each type is an exception: the dose distribution of the PtNP sample is shifted proximally by about 0.9 mm in comparison to the depth dose with the nonPtNP sample in the beam path (see magnification in figure 6(a)).

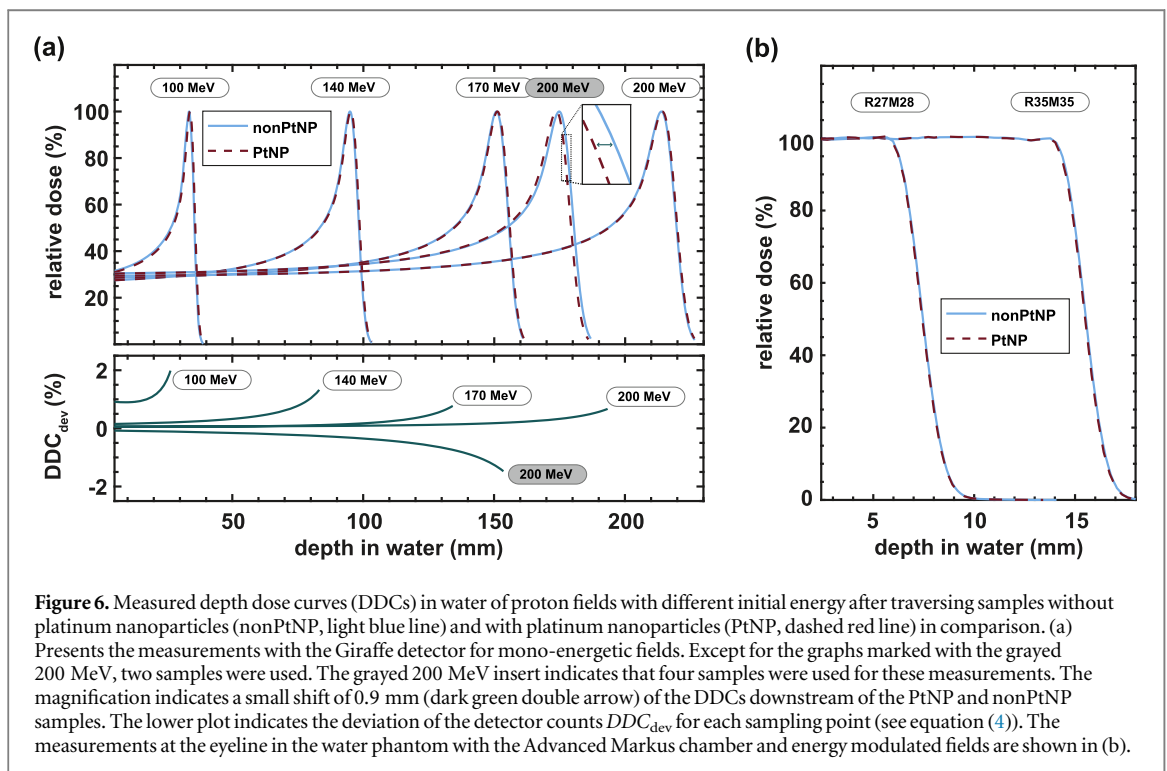
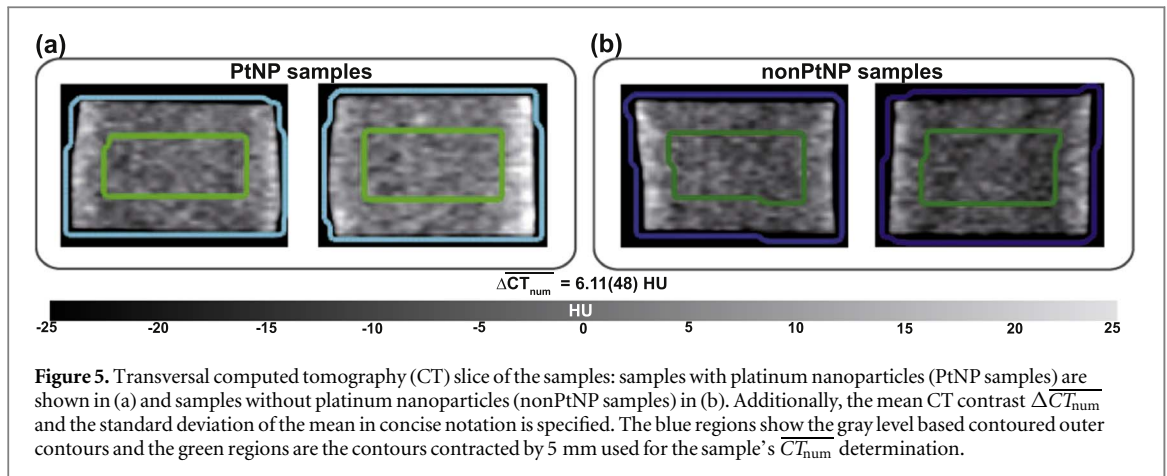


Table 1. Values of the dimensionless quantity WER_{ratio} (see equation (3)) with its standard uncertainty $\sigma_{WER_{ratio}}$ in concise notation.

Field configuration	Mono-energetic				Energy modulated		
	100 MeV	140 MeV	170 MeV	200 MeV	R27M28	R35M35	
Number of samples	2	2	2	2	4	1	1
WER_{ratio}	1.008(22)	1.008(22)	1.008(22)	1.008(22)	0.986(22)	0.999(22)	0.998(22)

The deviations of the DDCs' count values DDC_{dev} (see equation (4)) indicate positive values, for all except the measurement at 200 MeV with four stacked samples. But the deviations for each sampling point are smaller than 2% for depths less than the proximal 50% of the Bragg peak.

Table 1 presents the calculated WER_{ratio} values of the nonPtNP and PtNP samples based on equation (3) for the various field configurations and experimental setups of the depth dose measurements. The number of samples refers to the number per sample type, i.e. for PtNP and nonPtNP, respectively. The values of WER_{ratio} are consistent to 1 for all measurements, independent from the energy or the number of samples, including the one with four samples each at 200 MeV.

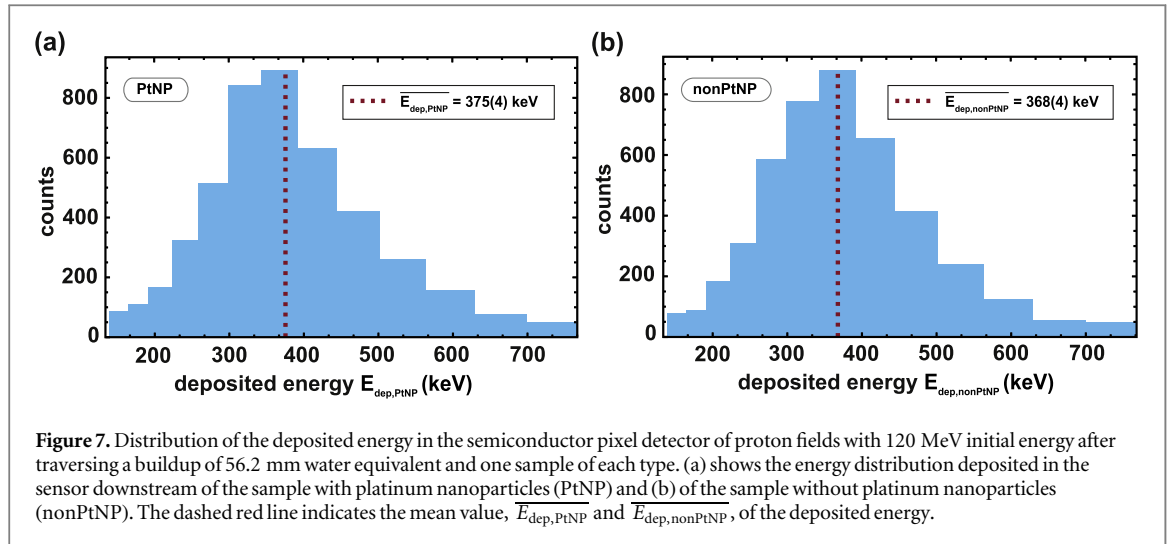


Figure 7. Distribution of the deposited energy in the semiconductor pixel detector of proton fields with 120 MeV initial energy after traversing a buildup of 56.2 mm water equivalent and one sample of each type. (a) shows the energy distribution deposited in the sensor downstream of the sample with platinum nanoparticles (PtNP) and (b) of the sample without platinum nanoparticles (nonPtNP). The dashed red line indicates the mean value, $\overline{E}_{\text{dep,PtNP}}$ and $\overline{E}_{\text{dep,nonPtNP}}$, of the deposited energy.

Table 2. Values of the ratio of the mean energy depositions $E_{\text{dep,ratio}}$ as well as the ratio of the spot sizes $\sigma_{\text{spot,ratio}}$ in the pixel detector.

Energy (MeV)	Setup	$\overline{E}_{\text{dep,sample}}$ (keV)		$E_{\text{dep,ratio}}$	$\sigma_{\text{spot,ratio}}$
		PtNP	nonPtNP		
100	3 samples stacked	510(6)	521(6)	$1.022(16)_{-0.028}^{+0.036}$	1.14(14)
		508(6)	520(6)	$1.024(16)_{-0.028}^{+0.036}$	1.02(10)
110	1 sample, absorber	556(6)	552(6)	$0.993(16)_{-0.011}^{+0.013}$	0.95(11)
		558(6)	555(6)	$0.995(16)_{-0.011}^{+0.013}$	1.13(11)
120	1 sample, absorber	377(5)	367(4)	$0.973(15)_{-0.005}^{+0.007}$	1.03(8)
		375(4)	368(4)	$0.981(16)_{-0.005}^{+0.007}$	0.96(5)
	4 samples stacked	382(5)	392(5)	$1.026(16)_{-0.023}^{+0.029}$	1.00(8)

3.3. Energy deposition and spot sizes

Figure 7 illustrates the distribution of the deposited energy in the sensor of a representative measurement with the pixel detector. These deposited energies of the initial protons in the sensor, $E_{\text{dep,PtNP}}$ and $E_{\text{dep,nonPtNP}}$, are given as histograms, where the bin size is optimized for the range of measured deposited energy in the sensor. The mean deposited energy in 200 μm silicon downstream of the PtNP sample is $\overline{E}_{\text{dep,PtNP}} = 375(4)$ keV and downstream of the nonPtNP sample $\overline{E}_{\text{dep,nonPtNP}} = 368(4)$ keV. These values are indicated by the dashed red line. Considering the experimental uncertainties of 1.09%, the values of the mean deposited energy downstream of the PtNP sample and the nonPtNP sample are comparable.

Table 2 summarizes the results of the ratio of the mean energy deposition $E_{\text{dep,ratio}}(E)$ in the pixel detector for each setup and initial proton energy (equation (5)). The number of samples refers to each sample type and the absorber in the setup indicates the additional buildup of $WET = 56.2$ mm. The standard uncertainty of $E_{\text{dep,ratio}}$ is written in concise notation and the second uncertainty analysis considering the different sample thicknesses is given as the upper and lower limit of the $\pm 1\sigma$ confidence interval. The values for the ratio of the mean deposited energy $E_{\text{dep,ratio}}$ downstream of the samples are approximately 1 for 100 and 110 MeV, whereas the values for $E_{\text{dep,ratio}}$ at 120 MeV are below 1 considering the experimental uncertainties. With additional consideration of the second uncertainty analysis for thickness variation, only the value of $E_{\text{dep,ratio}} = 0.973(15)_{-0.005}^{+0.007}$ is not consistent to 1 within the whole uncertainty budget.

While $E_{\text{dep,ratio}}$ is a measure of the mean values of the deposited energy, the statistical contribution of the shape of the energy distribution was tested under the assumption of equal mean values using the Mann-Whitney U test. This assumption was made because of the known differences in sample thicknesses. The test showed for all distributions of deposited energy downstream of the PtNP and nonPtNP samples of the respective measurement that they are not significantly different at $\alpha = 5\%$ significance level.

The determined values for the spot size ratio $\sigma_{\text{spot,ratio}}$ downstream of the PtNP and nonPtNP samples are also listed in table 2. The results show that the spot sizes agree within their experimental uncertainties except for the second measurement at 110 MeV. For the latter, the spots downstream of the nonPtNP sample are larger than the spots downstream of the PtNP sample, based on the definition in equation (6).

4. Discussion

This study establishes aspects in the energy domain for the underlying mechanisms behind the radiosensitizing effect of PtNPs in proton therapy. For this purpose, the ability of ROS generation of surfactant-free colloidal PtNPs of different concentrations was verified previously, indicating the potential of an enhanced therapeutic effect of radiotherapy by these PtNPs (figure 2). The fact that a higher concentration of PtNPs increases 2-OH-TA production can be attributed to the larger available surface area (Zwiehoff *et al* 2021). Manufactured gelatin samples without and with the same PtNPs of the highest demonstrated concentration were irradiated with protons and the downstream energy deposition was analyzed.

Based on the quantity WER_{ratio} and considering their uncertainties, no difference in the WER of samples with and without PtNPs in the beam path could be verified from the depth dose distributions (figure 6 and table 1). Since the WER is a measure of the stopping power for protons, the latter is not increased under the involvement of the platinum NPs used. Furthermore, the ratio of the mean deposited energies $E_{\text{dep,ratio}}(E)$ downstream of the PtNP and nonPtNP samples is approximately 1 for nearly all measurements with the pixel detector as presented in figure 7 and table 2. Thus, the stopping power for the protons in the silicon downstream of the PtNP and nonPtNP samples is also similar. According to the unchanged stopping power in the depth dose measurements and the measurements of the deposited energy in the pixel detector, the protons did not deposit more energy, and thus physical dose, in the presence of the PtNPs at the macroscopic scale.

The small difference in the DDCs downstream of the four stacked PtNP and nonPtNP samples and initial energy of 200 MeV in figure 6 might initially indicate an increased energy deposition due to the PtNPs. However, looking at WER_{ratio} , this difference is within the uncertainty, which is mainly dominated by the thickness determination of the samples (see table 1).

The additional analysis of the absolute DDCs (see lower part in figure 6) shows that there is a small deviation of less than 2% in the detector counts downstream of PtNP samples and nonPtNP samples up to a depth of the proximal 50% of the Bragg peak. An analysis in the peak region would lead to large deviations in the gradient due to small range mismatches. Normalization to R_{80} to compensate for these mismatches was not performed given the approaches of this study. According to the results, the total deposited energy of the protons after penetrating the PtNP and nonPtNP samples is comparable on a macroscopic scale. This indicates that the effect of nuclear interactions of protons and PtNPs is small, which otherwise could have been a further explanation for the radiosensitizing effect of PtNPs.

For a more detailed discussion of the results of $E_{\text{dep,ratio}}$ measured with the pixel detector, it is essential to consider the second uncertainty analysis, since $E_{\text{dep,ratio}}$ does not include the uncertainty on the sample thickness (see table 2). From the CT analysis (subsection 3.1) it is known that the samples may not be of equal thickness. Taking this into account, one value of $E_{\text{dep,ratio}}$ is outside the $\pm 1\sigma$ confidence interval, but nevertheless in the uncertainty of 2σ . Considering all measurements in this study, there is one result out of 14 measurements, that deviates more than the 1σ uncertainty, which is assumed to be statistically expected.

In order to compare the overall distribution of deposited energy in addition to the mean deposited energies, a Mann-Whitney U test was performed, which showed that the distributions are not significantly different ($\alpha = 5\%$), assuming the same mean value. The evaluation of the energy depositions indicates that the particles, which leave the different kind of samples, belong to the same population with a high level of confidence.

Due to the fact that for the measurements at 110 and 120 MeV the same buildup absorber was used, which results in different relative pixel detector depth positions in the Bragg curves, a possible position dependence of the detector in the depth domain may affect the sensitivity of the results. However, when comparing the measurements at 120 MeV with two different setups and detector depth positions, this effect seems unlikely. This is because the measurement with four samples, for which the detector position is at a larger depth, shows a value of $E_{\text{dep,ratio}}$ larger than 1 and thus does not indicate an increased proton energy deposition in the presence of PtNPs.

The spot sizes downstream of the PtNP and nonPtNP samples agree within their standard uncertainties for most measurements with the pixel detector, indicating that the presence of PtNPs does not affect the multiple Coulomb scattering of protons. The measurement at 110 MeV, where the spot sizes downstream of the various samples differ, also shows no increased scattering of protons by the PtNPs, since the spot size downstream of the nonPtNP sample is larger than that downstream of the PtNP sample. Thus, one of the measurements is not within the $\pm 1\sigma$ interval, which is statistically expected.

The presented macroscopic effects in the Bragg peak shape in Ahmad *et al* (2016), where gold nano-films with higher concentrations such as 5.5 mg ml^{-1} were used, could not be confirmed in this study (figure 6), which may suggest that nano-films are not comparable to NPs.

The dose increase from the radiosensitizing effect of metal NPs expected in other works is not evident in this study because it is assumed to be very localized around the NPs (Sicard-Roselli *et al* 2014, Wälzlein *et al* 2014,

Cho *et al* 2016). The deposited energy in the experiments presented here is measured macroscopically downstream of the samples and not microscopically in the immediate vicinity.

During the measurements with the Giraffe and the pixel detector, the samples were located in the entrance region, i.e. the clinically less relevant part, of the Bragg curve. However, the measurements at the eyeline with the modulated proton beam, where the samples were in the spread-out Bragg peak, led to the same results. Thus, the findings are generalizable on a macroscopic scale, regardless of the Bragg curve region in which the PtNPs are located. Further experiments should investigate whether there are influences at the microscopic scale, for example, due to the different proton LET, as described in Li *et al* (2016) for AuNPs.

The analysis of the sample parameters in a CT was performed on randomly selected samples. Two samples of each type were scanned. The calculated thickness ratio was assumed to apply for all PtNP and nonPtNP samples on average, respectively. Accordingly, deviations in the WER of the samples or the mean deposited energy downstream of them due to improperly corrected sample thickness may be explained if more than two samples were used for the measurement.

In addition, the CT scan has shown a higher contrast of the PtNP samples compared to the nonPtNP samples. Hence, the therapeutic use of metal NPs may affect clinical imaging like CT due to the high x-ray absorption coefficient of gold and platinum. Previous studies with AuNPs and higher concentrations than the one used in this study have already presented the possible use of NPs as nontoxic contrast agents in CT (Hainfeld *et al* 2013, Silvestri *et al* 2016, Han *et al* 2019). Furthermore, comparable CT contrast as an attenuation of about 8 HU was found with gadolinium at the same concentration (Kim *et al* 2018).

Based on investigations of the proton range, energy deposition and lateral scattering at various initial energies, this study indicates that the dose computed in the treatment planning of proton therapy is unaffected by PtNPs, although the planning CT would indicate an increased HU number. For a more detailed statement, three exemplary clinical treatment plans for brain tumors were used, to recalculate the original highly conformal dose distribution in the planning target volume assuming that the target volume would have the CT contrast of 6 HU more. However, the associated increase in mean density of 0.005 g cm^{-3} and stopping power based on the increased CT numbers compromises the dose coverage $D_{98\%}$ of the planning target volume below 0.2%. Moreover, contrary to expectations, the negative value for $\Delta D_{98\%}$ may be due to variations introduced by the voxel grid.

This study only involves physical experiments in which biological factors like cellular uptake or toxicity were not considered. In order to place large amounts of high-Z material in the beam path, a mass concentration of $300 \mu\text{g ml}^{-1}$ of colloidal NPs (0.03 wt% PtNPs in gelatin) with a mean diameter of $(40 \pm 10) \text{ nm}$ was used. These PtNPs with relatively high concentrations and a large diameter compared to similar studies (Zwiehoff *et al* 2021) were shown to lead to an increased concentration of damaging radicals in the form of 2-OH-TA by a factor of about 2 under proton irradiation compared to samples without PtNPs (figure 2). Thus, in this study, the focus was not on a clinically applicable concentration, but on a potentially high enhancement effect of proton therapy.

Based on these experiments, the radiosensitizing effect of PtNPs in proton therapy is not due to an increased proton energy deposition at the macroscopic scale. This confirms Dollinger's (Dollinger 2011) considerations that only a tiny fraction of the proton energy is transferred to the PtNPs themselves. Although the elementary mechanism behind the radiosensitizing effect of PtNPs in proton therapy remains an open question, these measurements finally provide further evidence for the catalytic effect of PtNPs in addition to previous ROS measurements (Zwiehoff *et al* 2021). For this reason, further chemical investigations could elucidate the underlying mechanisms of the radiosensitizing effect of NPs.

5. Conclusions

In this study, experimental evidence was provided that clinical proton fields do not deposit an increased amount of energy in the presence of ROS-producing PtNPs at the macroscopic scale. For this purpose, various measurements of proton stopping power downstream of $(40 \pm 10) \text{ nm}$ sized colloidal PtNPs at a concentration of $300 \mu\text{g ml}^{-1}$ were performed in comparison to samples without PtNPs. It was shown that there is macroscopically no enhanced effect in the water equivalent ratio as well as in the mean deposited energy downstream of the samples in the presence of PtNPs under these conditions. Moreover, the spot sizes were not affected by the protons' scattering at NPs. In clinical application, this corroborates uncomplicated treatment planning, since the dose in the target volume with NPs does not have to be additionally corrected.

As a result, this study could experimentally confirm mechanisms and theories already suspected in the literature regarding the radiosensitizing effect of noble metal NPs and serve as further evidence for the catalytic effect of NPs. Nevertheless, the employed types of experiment were not designed to explain the microscopic mechanism and cannot clarify the background of the radiosensitizing effect, but merely provide further insight into this highly interesting but not yet fully explored field of radiobiology.





Acknowledgments

The presented study was supported by the MERCUR-Stiftung graduate school “Präzisionsprotonentherapie—Praxisbezogene Physik und Chemie an der Schnittstelle zur Medizin” (grant number St-2019-0007) and the project “Synergistische Effekte von Gold-Nanopartikeln und Protonenbestrahlung bei der Behandlung von Hirntumoren im Kindesalter” (SYNGOPRO, grant number EFRE-0801289), which is funded by the European fund for regional development (EFRE). The authors would like to thank Horst Fischer and Michael Weber from Department of Dental Materials and Biomaterials Research RWTH Aachen University Hospital for gelation of the samples. In addition, the authors are grateful to the IBA PT and the WPE physics team for their experimental support. Special thanks to Benjamin Koska, for the commissioning data of the eyeliner. Furthermore, Valerie Hohm (TU Dortmund) is acknowledged for her support with the silicon detector measurements.

Conflicts of interest

The authors declare no conflict of interest.

ORCID iDs

C Behrends  <https://orcid.org/0000-0003-4148-1093>
I Schilling  <https://orcid.org/0000-0002-2437-3448>
S Zwiehoff  <https://orcid.org/0000-0001-8126-7329>
J Weingarten  <https://orcid.org/0000-0003-2165-871X>
K Kröninger  <https://orcid.org/0000-0001-9873-0228>
S Barcikowski  <https://orcid.org/0000-0002-9739-7272>
J Wulff  <https://orcid.org/0000-0001-8260-3523>
C Bäumer  <https://orcid.org/0000-0003-0512-1146>

References

- Ahmad R, Royle G, Lourenço A, Schwarz M, Fracchiolla F and Ricketts K 2016 Investigation into the effects of high-Z nano materials in proton therapy *Phys. Med. Biol.* **61** 4537–50
- Bäumer C, Koska B, Lambert J, Timmermann B, Mertens T and Talla PT 2015 Evaluation of detectors for acquisition of pristine depth-dose curves in pencil beam scanning *J. Appl. Clin. Med. Phys.* **16** 151–63
- Berger M, Coursey J, Zucker M and Chang J 2005 ESTAR, PSTAR, and ASTAR: computer programs for calculating stopping-power and range tables for electrons, protons, and helium ions (version 1.2.3) <http://physics.nist.gov/Star> [2022]
- Bethe H 1930 Zur Theorie des Durchgangs schneller Korpuskularstrahlen durch Materie *Ann. Phys.* **397** 325–400
- Bloch F 1933 Zur Bremsung rasch bewegter Teilchen beim Durchgang durch Materie *Ann. Phys.* **408** 285–320
- Butterworth K T, McMahon S J, Currell F J and Prise K M 2012 Physical basis and biological mechanisms of gold nanoparticle radiosensitization *Nanoscale* **4** 4830
- Cho J, Gonzalez-Lepera C, Manohar N, Kerr M, Krishnan S and Cho S H 2016 Quantitative investigation of physical factors contributing to gold nanoparticle-mediated proton dose enhancement *Phys. Med. Biol.* **61** 2562–81
- Dollinger G 2011 Comment on ‘Therapeutic application of metallic nanoparticles combined with particle-induced x-ray emission effect’ *Nanotechnology* **22** 248001
- Garcia-Sciveres M et al 2011 The FE-I4 pixel readout integrated circuit *Nucl. Instrum. Methods Phys. Res. A* **636** 155–9
- Grinstein S 2013 Overview of the ATLAS insertable B-layer (IBL) project *Nucl. Instrum. Methods Phys. Res. A* **699** 61–6
- Hainfeld J F, Dilmanian F A, Slatkin D N and Smilowitz H M 2008 Radiotherapy enhancement with gold nanoparticles *J. Pharm. Pharmacol.* **60** 977–85
- Hainfeld J F, Smilowitz H M, O’Connor M J, Dilmanian F A and Slatkin D N 2013 Gold nanoparticle imaging and radiotherapy of brain tumors in mice *Nanomedicine* **8** 1601–9
- Han X, Xu K, Taratula O and Farsad K 2019 Applications of nanoparticles in biomedical imaging *Nanoscale* **11** 799–819
- Joint Committee for Guides in Metrology 2008 Evaluation of measurement data—Guide to the expression of uncertainty in measurement *JCGM* **100**
- Kim J, Bar-Ness D, Si-Mohamed S, Coulon P, Bleviss I, Douek P and Cormode D P 2018 Assessment of candidate elements for development of spectral photon-counting CT specific contrast agents *Sci. Rep.* **8** 12119
- Kim J K, Seo S J, Kim H T, Kim K H, Chung M H, Kim K R and Ye S J 2012 Enhanced proton treatment in mouse tumors through proton irradiated nanoradiator effects on metallic nanoparticles *Phys. Med. Biol.* **57** 8309–23
- Kim J K, Seo S J, Kim K H, Kim T J, Chung M H, Kim K R and Yang T K 2010 Therapeutic application of metallic nanoparticles combined with particle-induced x-ray emission effect *Nanotechnology* **21** 425102
- Klein C A 1968 Bandgap dependence and related features of radiation ionization energies in semiconductors *J. Appl. Phys.* **39** 2029–38
- Lacombe S, Porcel E and Scifoni E 2017 Particle therapy and nanomedicine: state of art and research perspectives *Cancer Nanotechnol.* **8** 9
- Li S et al 2016 LET-dependent radiosensitization effects of gold nanoparticles for proton irradiation *Nanotechnology* **27** 455101
- Mesbahi A 2010 A review on gold nanoparticles radiosensitization effect in radiation therapy of cancer *Rep. Pract. Oncol. Radiother.* **15** 176–80
- Polf J C, Bronk L F, Driessen W H P, Arap W, Pasqualini R and Gillin M 2011 Enhanced relative biological effectiveness of proton radiotherapy in tumor cells with internalized gold nanoparticles *Appl. Phys. Lett.* **98** 193702

- Schlathöler Lacombe *et al* 2016 Improving proton therapy by metal-containing nanoparticles: nanoscale insights *Int. J. Nanomed.* **11** 1549–56
- Schuemann J *et al* 2020 Roadmap for metal nanoparticles in radiation therapy: current status, translational challenges, and future directions *Phys. Med. Biol.* **65** 21RM02
- Le Sech C, Kobayashi K, Usami N, Furusawa Y, Porcel E and Lacombe S 2012 Comment on 'Enhanced relative biological effectiveness of proton radiotherapy in tumor cells with internalized gold nanoparticles'. [Appl. Phys. Lett. 98, 193 702 (2011)] *Appl. Phys. Lett.* **100** 026101
- Sicard-Roselli C, Brun E, Gilles M, Baldacchino G, Kelsey C, McQuaid H, Polin C, Wardlow N and Currell F 2014 A new mechanism for hydroxyl radical production in irradiated nanoparticle solutions *Small* **10** 3338–46
- Silvestri A, Zambelli V, Ferretti A M, Salerno D, Bellani G and Polito L 2016 Design of functionalized gold nanoparticle probes for computed tomography imaging *Contrast Media Mol. Imaging* **11** 405–14
- Slopsema R L, Mamelui M, Zhao T, Yeung D, Malyapa R and Li Z 2013 Dosimetric properties of a proton beamline dedicated to the treatment of ocular disease *Med. Phys.* **41** 011707
- Smith C L, Best S P, Gagliardi F, Tominaga T and Geso M 2017 The effects of gold nanoparticles concentrations and beam quality/LET on dose enhancement when irradiated with x-rays and protons using alanine/EPR dosimetry *Radiat. Meas.* **106** 352–6
- Usami N, Furusawa Y, Kobayashi K, Frohlich H, Lacombe S and Sech C L 2005 Fast He²⁺ ion irradiation of DNA loaded with platinum-containing molecules *Int. J. Radiat. Biol.* **81** 515–22
- Usami N, Furusawa Y, Kobayashi K, Lacombe S, Reynaud-Angelin A, Sage E, Wu T D, Croisy A, Guerquin-Kern J L and Sech C L 2008 Mammalian cells loaded with platinum-containing molecules are sensitized to fast atomic ions *Int. J. Radiat. Biol.* **84** 603–11
- Waag F, Streubel R, Gökce B and Barcikowski S 2021 Synthesis of gold, platinum, and gold-platinum alloy nanoparticle colloids with high-power megahertz-repetition-rate lasers: the importance of the beam guidance method *Appl. Nanosci.* **11** 1303–12
- Wälzlein C, Scifoni E, Krämer M and Durante M 2014 Simulations of dose enhancement for heavy atom nanoparticles irradiated by protons *Phys. Med. Biol.* **59** 1441–58
- Weingarten J 2012 ATLAS IBL sensor qualification *J. Instrum.* **7** C01039
- Zhang R and Newhauser W D 2009 Calculation of water equivalent thickness of materials of arbitrary density, elemental composition and thickness in proton beam irradiation *Phys. Med. Biol.* **54** 1383–95
- Zwiehoff S, Johnny J, Behrends C, Landmann A, Mentzel F, Bäumer C, Kröniger K, Rehbock C, Timmermann B and Barcikowski S 2021 Enhancement of proton therapy efficiency by noble metal nanoparticles is driven by the number and chemical activity of surface atoms *Small* **18** 2106383